An Imaging Search for Circumstellar Companions of Sirius B

Miles Lucas [ID],[1] Michael Bottom [ID],[2] Garreth Ruane [ID],[3] and Sam Ragland [ID][4]

[1]*Institute for Astronomy, University of Hawaii at Manoa, 2680 Woodlawn Dr, Honolulu, HI 96822, USA*
[2]*Institute for Astronomy, University of Hawaii at Hilo, 640 N Aohoku Pl, Hilo, HI 96720, USA*
[3]*Jet Propulsion Laboratory, California Institute of Technology, 4800 Oak Grove Dr, Pasadena, CA 91109, USA*
[4]*W.M. Keck Observatory, 65-1120 Mamalahoa Hwy, Waimea, HI 96743, USA*

ABSTRACT

We present deep imaging of Sirius B, the closest and brightest white dwarf. We use Keck/NIRC2 in Lp-band (3.776 μm) across three epochs in 2020 using the technique of angular differential imaging. We reach sub-Jupiter sensitivities and sub-AU separations, reaching $3.5\,M_J$ at $0.25\,AU$ down to a sensitivity of $0.6\,M_J$ at $1.5\,AU$. The uncertainty in mass sensitivity is below $0.1\,M_J$ due to the precisely known Sirius B system age. Consistent with previous results, we do not detect any companions around Sirius B.

1. INTRODUCTION

High-contrast imaging (HCI) is a powerful technique for discovering and characterizing exoplanets. Probing the architecture, formation, and atmospheres of planets directly is necessary for advancing substellar companion formation and evolution theory. Imaging a planet is challenging, however. The typical astrophysical flux ratios (contrast) for a Sun-Jupiter analog in the near-infrared (NIR) are $\sim 10^{-8}$, and for a Sun-Earth system are $\sim 10^{-10}$ (Traub & Oppenheimer 2010). Thermal emission from exoplanets peaks in the infrared and is well into the Rayleigh-Jeans limit of the star, decreasing contrast compared to the visible or ultraviolet. In addition, the close angular separations of planets make it difficult to detect them over the diffraction pattern of their host and other noise sources.

White dwarfs (WD) are interesting targets for direct imaging- they are 3 to 4 orders of magnitude fainter than their main-sequence (MS) progenitors which reduces the contrast necessary to detect a companion. In addition, the relative lack of spectral features of WDs makes them imprecise targets for radial velocity analysis. The intrinsic faintness of WDs proves challenging for all detection methods; this is exacerbated on ground-based telescopes which require significant signal-to-noise (S/N) to operate their adaptive optics (AO) facilities. This implicitly limits searches of WDs to the $\sim 100\,pc$ neighborhood.

Corresponding author: Miles Lucas
mdlucas@hawaii.edu

Little is known about post-MS planetary evolution, however, planets that are tenuous enough to survive the red giant and asymptotic giant phases of its host are interesting laboratories for planetary formation pathways as showcased by recent discoveries like giant planet candidate WD 1856+534b (Vanderburg et al. 2020).

In this work, we briefly review post-MS planetary formation theory (section 2) and discuss the Sirius system, specifically bright WD Sirius B, as potential exoplanet hosts (section 3). In section 4, section 5, and section 6 we describe our observations of Sirius B in 2020, along with the subsequent analysis. Finally, in section 7 we discuss the implications of our observations for planetary formation theory and future work.

2. POST-MS EVOLUTION

There is limited knowledge of planetary systems around evolved stars. Burleigh et al. (2002); Veras (2016) suggest exoplanets on initially wide ($>5\,AU$) orbits around intermediate-mass stars will survive expansion during the RGB phase. Planets very close to the Roche limit of the expanding red giant can still be shredded by tidal forces despite escaping engulfment, although the tidal forces are negligible on planets that are far from the Roche limit (and readily escape engulfment) (Nordhaus & Spiegel 2013). During the AGB phase, stellar mass loss adiabatically expands the orbit of the planet by a maximum factor of $M_{*,MS}/M_{*,WD}$ (Jeans 1924). In addition to *first-generation* planets, there are potential methods for *second-generation* planets to form after the violent RGB and AGB phases (Perets 2010).

The first search for substellar companions around white dwarfs was conducted by Probst (1983). They searched for infrared (IR) excess in their spectral energy distributions (SED) using broadband photometry. The IR excess would be indicative of thermal emission of faint material around the star, such as a circumstellar disk or giant planet. They studied ∼100 white dwarfs but found no companions. The same method was applied by Zuckerman et al. (2010), who found excess IR emission around white dwarf G29-38. The emission was determined to be from a dust disk (Telesco et al. 1990), which was associated with accretion onto the white dwarf's surface, polluting the stellar atmosphere (Koester et al. 1997). It is estimated that while a third of white dwarfs are polluted, only a few percent have IR excesses (Bonsor et al. 2017). Skemer & Close (2011) suggested stellar radiation from stars hotter than 15.000 K would sublimate dust, therefore, suppressing any IR excess.

Imaging is well-suited for studying evolved planetary systems, yet to date, only one planet has been imaged around a white dwarf. Luhman et al. (2011) discovered a companion around WD 0806-661B with a mass of $7\,M_{\rm J}$ on a wide 2500 AU orbit using Spitzer. The "Degenerate Objects around Degenerate Objects" survey (DODO; Hogan et al. 2009) observed 29 white dwarfs with Gemini/NIRI and VLT/ISAAC, reaching an average upper limit around ∼$8\,M_{\rm J}$ beyond 35 AU. The young white dwarf GD 50 was observed using the extreme AO instrument SPHERE at the VLT (Xu et al. 2015), reaching sensitivity limits of $4\,M_{\rm J}$ at 6.2 AU.

3. SIRIUS B AND THE SIRIUS SYSTEM

A particularly fascinating target is Sirius B, the closest and brightest white dwarf. The Sirius system is the 7th closest to the sun at 2.6 pc, consisting of Sirius A, a -1.35 magnitude A1Vm star known for being the brightest, and Sirius B, a DA2 white dwarf with a 50 yr orbit (Collaboration et al. 2016; Bond et al. 2017; Collaboration et al. 2021). As mentioned previously, the proximity and faintness of Sirius B (compared to a MS star) make it compelling for imaging. Additionally, the young system age (∼225 Myr) means any giant planets would still retain much of their latent formation heat, increasing their luminosity in the IR (Fortney et al. 2010).

A common problem in direct imaging is determining planetary masses from photometry using planetary atmosphere evolution grids. This method of interpolation depends on the stellar age, the stellar photometry, and the distance to the system. Determining stellar ages is quite difficult and sometimes impossible, and is often the largest source of uncertainty when interpolating planetary masses. Age uncertainty exponentially affects young systems (<1 Gyr) due to the rapid cooling of giant planets. Sirius B avoids these pitfalls due to its unusually high age precision, primarily derived from accurate dynamical masses.

The dynamical masses are determined through astrometric studies; the first study of Sirius was performed by Bessel (1844), who recognized wobbles in the proper motion of Sirius A caused by a "dark satellite". This dark satellite was visually confirmed in Bond (1862) as Sirius B. Adams (1915) took the first spectral measurements of Sirius B and found it to be similar to a MS early A-type star, despite its faintness, which we now know to be typical of white dwarf spectra.
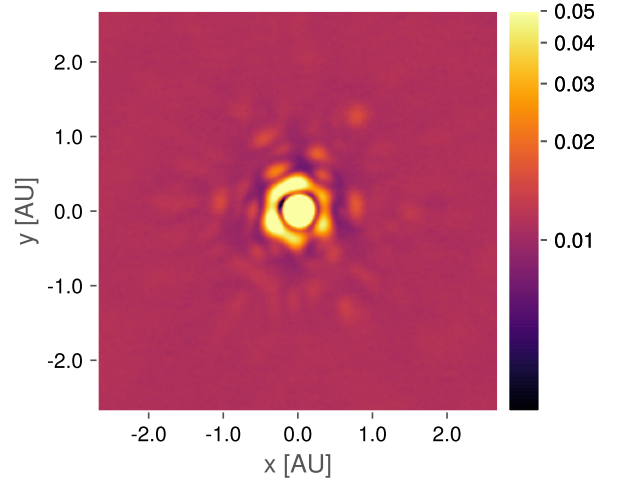
Initial astrometric measurements suggested a 50 year orbital period for Sirius B (Auwers 1864). van den Bos (1960); Gatewood & Gatewood (1978) were the first to estimate dynamical masses using compilations of photographic plates from Lick and Yerkes observatories. Bond et al. (2017) greatly refined the orbital solution using a compilation of historical data and Hubble Space Telescope (HST) data, which gave dynamical masses of $(2.063 \pm 0.023)\,M_{\odot}$ and $(1.018 \pm 0.011)\,M_{\odot}$ for A and B, respectively. A companion around Sirius B would be affected by the orbit of Sirius A, and this constrained three-body system has been studied numerically (Holman & Wiegert 1999). Bond et al. (2017) calculate the longest period stable companion around Sirius B is 1.79 yr, which corresponds to a 1.5 AU circular orbit.

To find the total age of Sirius B, Bond et al. (2017) used isochrones to constrain the cooling age (126 Myr), first. Applying the initial-final mass relation (IFMR) of white dwarfs (Cummings et al. 2016) the estimated progenitor mass of Sirius B is between $5\,M_{\odot}$ to $5.6\,M_{\odot}$, which, when combined with stellar evolution codes, yielded total system ages between 226 Myr to 228 Myr with an uncertainty of about ±10 Myr (Bond et al. 2017). An age uncertainty of ∼1% is exceptional compared to the ∼10% or worse of stars found in young moving groups, not to mention many stars cannot be precisely dated at all.

The first modern imaging study searching for companions around Sirius B was Schroeder et al. (2000) who used the HST wide-field planetary camera (WFPC) at 1 µm. Around the same time Kuchner & Brown (2000) searched in a narrower field of view (FOV) with HST/NICMOS at 1 µm. These studies combined had a sensitivity down to ∼$10\,M_{\rm J}$ at 5.3 AU (2″). Bonnet-Bidaud & Pantin (2008) used the ground-based ESO/ADONIS instrument in J, H, and Ks-band and reached a sensitivty of ∼$30\,M_{\rm J}$ at 7.9 AU (3″). Skemer & Close (2011) used mid-IR (up to 10 µm) observations

Table 1. Parameters of the Sirius system adopted in this study.

parameter	value	unit	ref.
t_{sys}	226	Myr	B17; C18
π	374.50 ± 0.23	mas	G21a
d	2.6700 ± 0.0016	pc	G21a
Sirius A			
$M_\star$	2.063 ± 0.023	$\mathrm{M}_\odot$	B17
Sirius B			
$M_\star$	1.018 ± 0.011	$\mathrm{M}_\odot$	B17
t_{WD}	125	Myr	B17; C18
m^{Lp}	9.01 ± 0.16		BB08
M^{Lp}	11.88 ± 0.16		BB08; G21a
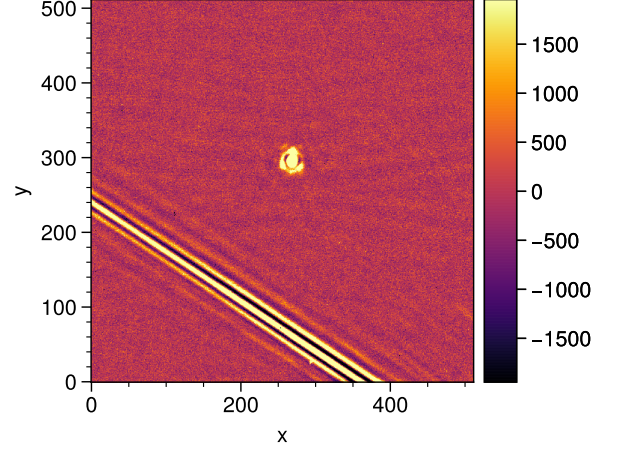
Figure 1. A diffraction spike sweeping across a calibrated science frame of Sirius B from the first epoch. This shows the strong scattered light effects of Sirius A and how they affect the FOV of Sirius B $11''$ away.

from Gemini/T-ReCs which ruled out evidence for any infrared excess around Sirius B. Thalmann et al. (2011) used Subaru/IRCS at $4.05\,\mu\mathrm{m}$ reaching detection sensitivities of $6\,\mathrm{M_J}$ to $12\,\mathrm{M_J}$ at $1''$. Recently, Pathak et al. (2021) took simultaneous mid-IR observations ($10\,\mu\mathrm{m}$) at VLT/VISIR of Sirius A (through a coronagraph) and B. Because of the simultaneous observation, their contrast depended on which region of the FOV was tested. Their average sensitivity is $\sim 2.5\,\mathrm{M_J}$ at $1\,\mathrm{AU}$, and their best sensitivity (from the "inner" region) is $\sim 1.5\,\mathrm{M_J}$ at $1\,\mathrm{AU}$.

In this work, we report direct images of Sirius B with Keck/NIRC2. The rest of the manuscript is organized as follows: section 4 describes our target and observing strategy, section 5 describes the processing and analysis techniques used, and section 6 describes our results.

4. OBSERVATIONS

Despite Sirius B being the brightest white dwarf in the sky, it is still 10 magnitudes fainter than Sirius A, making it a technically challenging target, especially on ground-based telescopes. We directly imaged Sirius B with Keck/NIRC2 in Lp-band ($3.776\,\mu\mathrm{m}$) using the narrow camera ($10\,\mathrm{mas\,px^{-1}}$; $2.5'' \times 2.5''$) across three epochs in 2020 (table 2). Our first attempt to observe Sirius B failed due to the strong scattered light from Sirius A. The adaptive optics (AO) calibration failed when the scattered light from Sirius A would sweep into the

Figure 2. The median frame from the second epoch showing the instrumental PSF. The inner core has a FWHM of $\sim 76\,\mathrm{mas}$. The speckle pattern is shown in the blobs surrounding the first ring, with roughly 6-way radial symmetry corresponding to the hexagonal shape of the primary mirror.

FOV of the wavefront sensor (WFS). Similarly, trying to deploy the focal-plane vortex coronagraph (Serabyn et al. 2017) failed when the coronagraphic pointing control algorithm, `QACITS` (Huby et al. 2017), performed erratically in the presence of the scattered light. We did not try coronagraphy for the remaining observations. Vigan et al. (2015, §2) reported similar issues in their attempts to image Sirius B coronagraphically using VLT/SPHERE. In order to overcome these obstacles, we decided to try using Sirius A as the AO guide star and off-axis guiding to Sirius B.

Table 2. Observing parameters for the three epochs of data. All observations were carried out using the NIRC2 narrow camera (10 mas px^{-1}; 2.5″×2.5″) in Lp-band (3.776 μm). Observation time is based on the frames that were selected for processing. Seeing values were measured at 0.5 μm using a differential image motion monitor (DIMM) and averaged over the observing session. Seeing values, temperature, and water vapor measurements were all taken from the Maunakea weather center forecast archive.

Date observed	Sirius B offset (″)	Sirius B PA (°)	Obs. time (hr)	FOV rotation (°)	FWHM (mas)	Seeing (″)	Temp (°C)	PWV (mm)
2020-02-04	11.20	67.90	1.44	60.1	79.9	0.936	0.0	0.7
2020-11-21	11.27	66.42	2.91	91.4	76.4	0.871	0.8	3.5
2020-11-28	11.27	66.38	2.44	80.4	82.2	1.23	-1.5	3.0

The Keck AO system (Wizinowich et al. 2000) was saturated by Sirius A, so we attenuated the flux using a narrow laser-line filter in the WFS. While still bright (appearing like a ∼5 magnitude star on the WFS), this was enough attenuation to close the AO loop. From here, we slewed off-axis using the separations and position angles calculated in table 2 from the orbital parameters in Bond et al. (2017). In this mode, we noticed higher than usual drift in the focal plane, requiring manually recentering the target every 5 or 10 minutes.

During each observation, we took dark frames and sky-flat frames for calibration. All observations were taken with the telescope's field rotator set to track the telescope pupil in order to exploit the natural rotation of the sky via angular differential imaging (ADI; Marois et al. 2006).

5. ANALYSIS

5.1. *Pre-processing*

The raw images from NIRC2 required pre-processing before analyzing them for companions. For each epoch, we applied a flat correction using calibration frames captured during observing. We also removed bad pixels using a combination of `L.A.Cosmic` (van Dokkum 2001) and an adaptive sigma-clipping algorithm. We removed sky background using a high-pass median filter with a box size of 31 pixels. For both the November epochs we tried exploiting the large focal plane drifts by dithering between two positions in order to simplify background subtraction, but this ended up performing worse than the high-pass filter. At this point frames were manually selected to remove bad frames, especially those with diffraction spikes from Sirius A within a few hundred pixels, like in fig. 1. Then, each good frame was co-registered to sub-pixel accuracy using the algorithm presented in Guizar-Sicairos et al. (2008), followed by fitting each frame with a Gaussian PSF to further increase centroid accuracy.

The co-registered frames were shifted to the center of the FOV and cropped to the inner 200 pixels. With a pixel scale of 10 mas the crop corresponds to a maximum separation of 1″ or a projected separation of 2.7 AU. All the frames were stacked into data cubes for each epoch. We also measure the parallactic angle of each frame, including corrections for distortion effects following Yelda et al. (2010). For each epoch, we measure the full-width at half-maximum (FWHM) of the stellar PSF for use in post-processing by fitting a bivariate Gaussian model to the median frame from each data cube (fig. 2). All of the pre-processing code is available in Jupyter notebooks in a GitHub repository (section 7.1).

5.2. *Post-processing*

By taking data with the field rotator disabled (ADI), the point-spread function (PSF) will not appear to rotate while any potential companion will appear to rotate. This reduces the probability of removing companion signal when we subtract the stellar PSF model. After subtraction, the frames are derotated by their parallactic angle and combined with a weighted sum (Bottom et al. 2017), which reduces the pixel-to-pixel noise as the number of frames in the data cube increases.

For this analysis, we used four ADI algorithms for modeling and subtracting the stellar PSF: median subtraction (Marois et al. 2006), principal component analysis (PCA, also referred to as KLIP; Soummer et al. 2012), non-negative matrix factorization (NMF; Ren et al. 2018), and fixed-point greedy disk subtraction (GreeDS; ?Pairet et al. 2020). The median subtraction and PCA methods were also applied in an annular method, where we modeled the PSF in annuli of increasing separation, discarding frames that have not rotated at least 0.5 FWHM (Marois et al. 2006). These algorithms are implemented in the open-source `ADI.jl` Julia package (Lucas & Bottom 2020).

We used three metrics available in `ADI.jl` to determine the performance of each algorithm, the signal-to-noise ratio (S/N) significance map, the standardized tra-
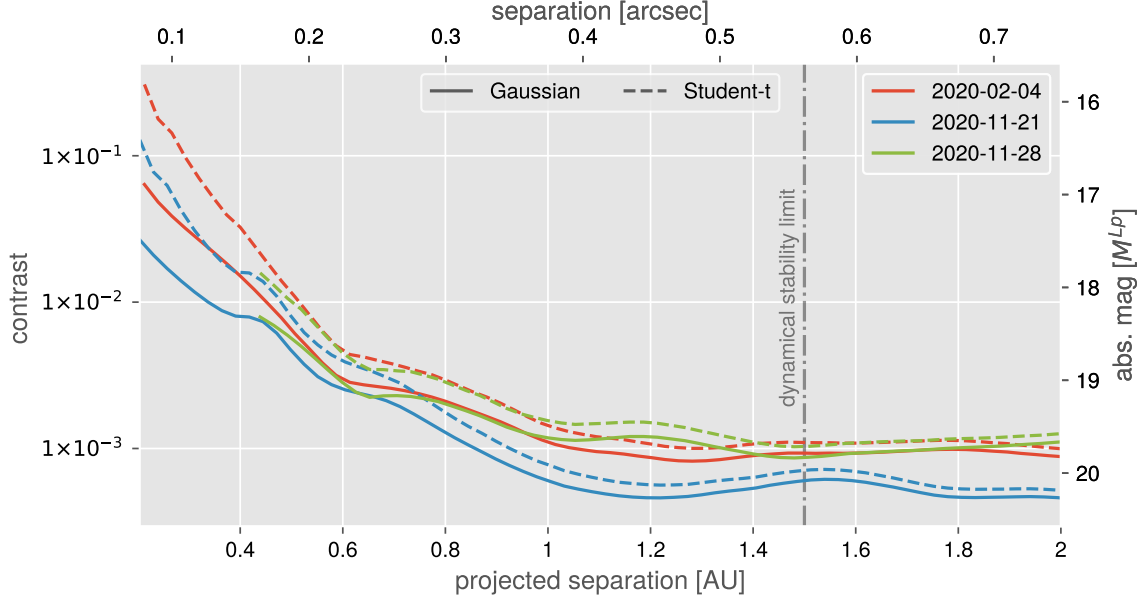
Figure 3. The contrast curves for the best performing algorithm from each epoch. The solid lines are the Gaussian 5σ contrast curves and the dashed lines are the Student-t corrected curves. The expected upper limit for a dynamically stable orbit of 1.5 AU is plotted as a vertical dashed line. The annular PCA curve is cut off because the innermost annulus has a contrast value greater than 1, which means even a 100 S/N companion would not be detectable with 5σ significance.
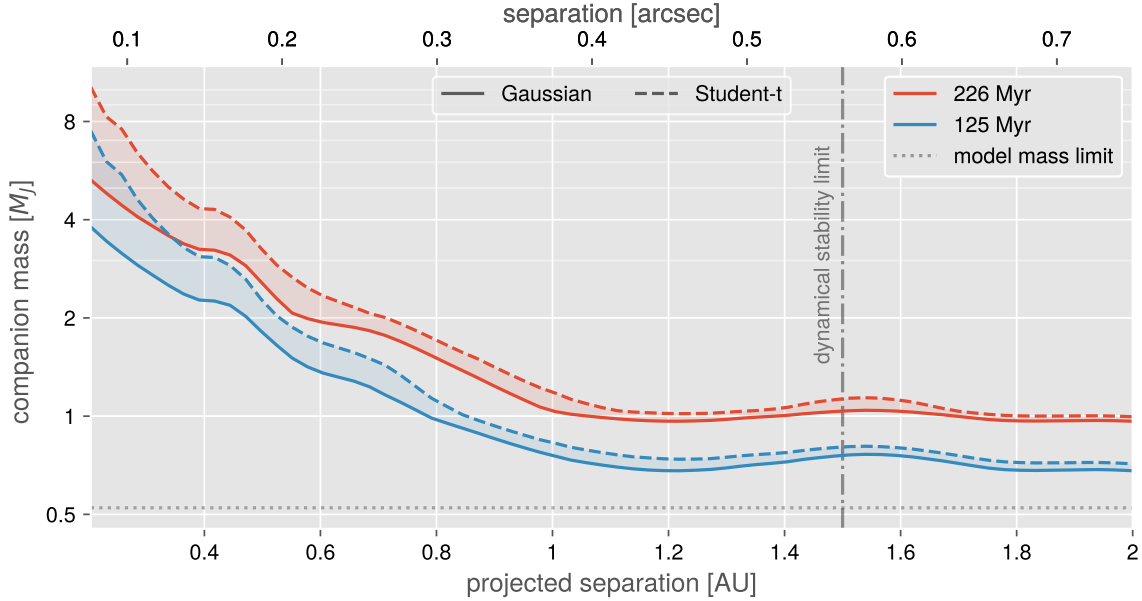

Figure 4. Mass sensitivity curves derived from the 2020-11-21 epoch, which has the best contrast. The solid lines are the Gaussian 5σ detection limits and the dashed lines are the Student-t corrected limits. The two ages represent the ages of the two potential formation pathways, one of which is the system age (226 Myr), the other is the WD cooling age of Sirius B (125 Myr). The limits are calculated assuming an Lp apparant magnitude for Sirius B of 9.01 and converting contrast into absolute magnitudes. The absolute magnitudes are converted to masses using the ATMO2020 isochrone grid with non-equilibrium chemistry and weak convective mixing. The lower mass limit of the ATMO2020 grid is plotted with a horizontal dashed line and the expected upper limit for dynamically stable orbits of 1.5 AU is plotted with a vertical dashed line.
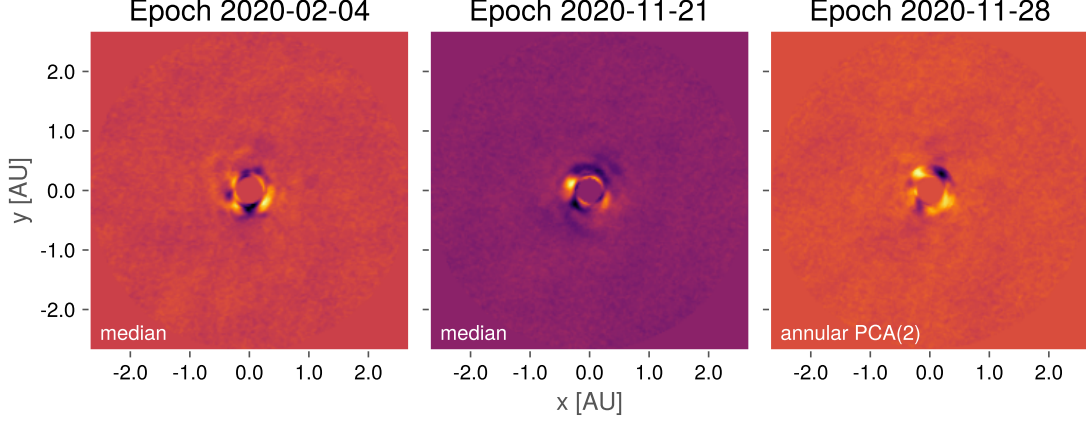
Figure 5. The flat residuals of each epoch after PSF subtraction, derotating, and collapsing. The inner full-width at half-maximum (FWHM) is masked out for each frame.
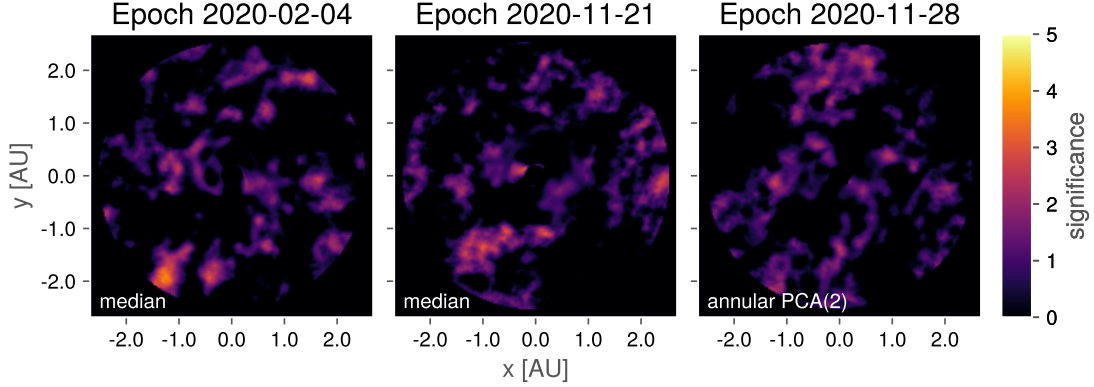
Figure 6. The *significance* maps for each epoch accounting for small-sample statistics (**?**). Typically a critical value for detection is 5. The inner full-width at half-maximum (FWHM) is masked out for each map.
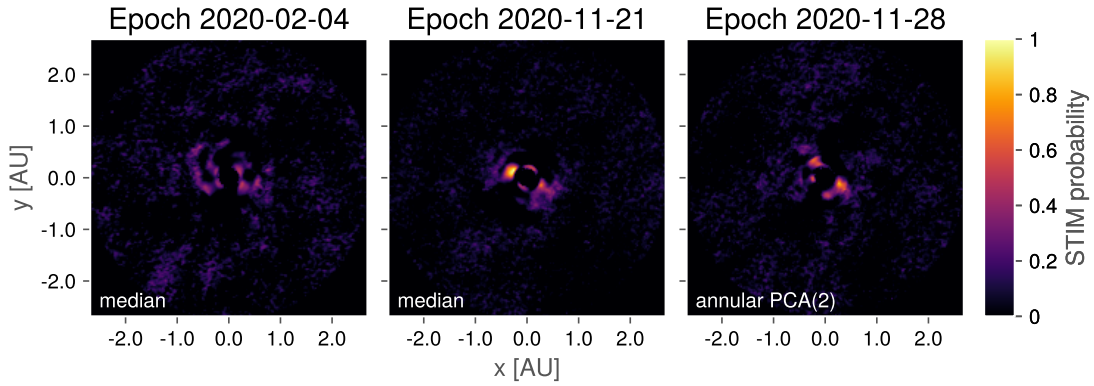

Figure 7. The STIM maps for each epoch calculated from each residual cube. The STIM probability has a typical cutoff threshold of 0.5 for significant detections. The inner full-width at half-maximum (FWHM) is masked out for each map.

jectory intensity mean map (STIM map; Pairet et al. 2019), and the contrast curve. The significance and STIM maps assign a likelihood to each pixel for the presence of a companion using different assumptions of the residual statistics. The contrast curve determines the sensitivity of a 5σ statistical detection through repeated injection and retrieval of planetary signal as processed by one of the ADI algorithms above. We calculate both the Gaussian contrast and the Student-t corrected contrast, which accounts for the small-sample statistics in each annulus (Mawet et al. 2014). The collapsed residual frames along with the above metrics for each algorithm for each epoch are in section A.

A common problem when using subspace-driven post-processing algorithms like PCA, NMF, or GreeDS is choosing the size of the subspace (i.e., the number of components). For PCA, NMF, and GreeDS algorithms, we increased the number of components from 1 to 10, creating a residual cube for each iteration. We chose 10 for the maximum number of components because we saw a dramatic decline in contrast sensitivity after the first few components (fig. 12). In our analysis we employed the STIM largest intensity mask map (SLIM map; Pairet 2020) as an ensemble statistic. The SLIM map calculates the average STIM map from many residual cubes along with the average mask of the N most intense pixels in each STIM map. A real companion ought to be present in many different residual cubes from the same dataset, so this ensemble approach can give us a probability map without predetermining the number of components. The collapsed residual frames, average STIM map, SLIM map, and contrast curves for each epoch for each of the above algorithms are in section A. All of the code used for this analysis is available in a GitHub respository (section 7.1).

6. RESULTS

We determined the best-performing algorithms for each epoch using the contrast curves described in section 5. For the first two epochs, full-frame median subtraction had the best contrast at almost all separations. For the last epoch annular PCA subtraction with 2 principal components and a rotation threshold of 0.5 FWHM produced the best contrast at close separations ($0.2''$ to $0.4''$) and had similar performance to other algorithms beyond $0.4''$. The innermost annulus from this algorithm has greater than 1 contrast which implies a 100 S/N companion would not be detected with 5σ significance. The contrast for this innermost annulus is therefore not plotted. The collapsed residual frames from each epoch are shown in fig. 5, along with the Gaussian significance maps (fig. 6) and STIM maps (fig. 7).

The reduced images do not show consistent or significant evidence for a substellar companion. The STIM probability maps for the 2020-11-21 and 2020-11-28 epochs suggest evidence for some blobs ~0.3 AU ($0.13''$; 1.6 FWHM) from the center. The February epoch also shows a blob at a similar separation in the reduced image which does not appear in the STIM map. The lack of statistical evidence in the February epoch and the significance maps as well as the proximity to the central star both reduce the probability of these blobs being true companions. Nonetheless, we estimated astrometry for blobs from each epoch (table 3) and tried fitting Keplerian orbits using the "Orbits for the Impatient" algorithm (OFTI; Blunt et al. 2017). We generated 10^4 orbits, none of which contained the points from each epoch (section B). We take this as direct evidence against the blobs being substellar companions of any kind.

6.1. *Companion Mass Detection Limits*

The contrast maps from the best performing algorithm for each reduction are shown in fig. 3. We determine the limiting sensitivities in terms of the planetary mass by first calculating the contrast-limited magnitude using an Lp-band magnitude for Sirius B of 9.1 (adapted from **?**). Then we used 225 Myr for the system age to interpolate the planetary mass using the AMES-Cond evolutionary grid and atmosphere models . The high precision of the Sirius system's age reduces uncertainty when interpolating planetary mass from the evolutionary grids (see section 1). We also tested using the newer SONORA grid , but the differences compared to AMES-Cond were less than the mean uncertainty from age. The best performing epoch was on the night of 2020-11-21, which managed to reach an exceptional sensitivity of $3.5\,M_J$ at 0.25 AU ($0.09''$) in the speckle limited regime and ultimately $0.6\,M_J$ at 1.5 AU ($0.38''$) in the background limited regime.

7. CONCLUSIONS

In closing, the Sirius system is one of the most well studied in history, with Sirius B being the target of companion searches from the visible to the IR. While it is highly unlikely a first-generation planet survived post-MS evolution, imaging efforts have gradually increased the sensitivity to second-generation planets. In this work, we present high-contrast images of Sirius B in the near-IR. Our sensitivity limits are the best that have been reached for Sirius B so far, reaching $0.6\,M_J$ at 1.5 AU, the outer limit for dynamically stable orbits. Our observations also show how the high precision of the parameters of the Sirius system directly benefits the sensitivity to planets. Particularly, the low age uncertainty

of Sirius B keeps our mass uncertainty below $0.1\,M_J$. Despite the high sensitivity of this study, we found no appreciable evidence for a companion around Sirius B, consistent with previous results. This non-detection furthers evidence against a second-generation planet migrating or forming within the Sirius system (Vigan et al. 2015).

For future work, we consider two avenues for followup. As mentioned in section 6, optical observations using an instrument like Subaru/VAMPIRES . Optical observations can look for disks in the Rayleigh-scattering regime, which is not readily probed by IR observations. Furthermore, the polarimetric differential observation modes of both instruments allow for nearly diffraction-limited imaging, down to 10s of milliarcseconds.

Followup in the IR from space-based telescopes would increase the sensitivity of the observations due to the absence of background emission from Earth's atmosphere. For example, using JWST/NIRCAM in long-wavelength imaging mode has a limiting magnitude of $\sim$25 in the F480M filter, which would easily reach the model mass sensitivity limits at $>0.3''$ without saturation . The pixel scale $(0.06\,''\,\mathrm{px}^{-1})$ and PSF size $(\sim0.3'')$ would still probe down to 0.8 AU. Observations would be complicated by the scattered light from Sirius A, which could affect the fine-pointing control or worsen the background sensitivity. In the end, our ground-based observations are already quite close to the atmospheric model grid limits, raising the concern of diminishing returns. Planetary atmosphere models must improve, before fully reaping the benefits of the additional sensitivity of space-based observations.

7.1. *Data and Code Availability*

All of the code used for pre-processing data, reducing data, and generating the figures is available under an open-source license in a GitHub repository[1]. This code includes all of the scripts for generating each figure in this manuscript. The pre-processed data cubes and parallactic angles are available on Zenodo under an open-source license[2]. We hope that this improves the reproducibility of the work as well as providing data for future investigations. Please reach out to the corresponding author for further inquiries regarding data and code availability.

Facility: Keck:II (NIRC2)

Software: ADI.jl (Lucas & Bottom 2020), astropy (?Astropy Collaboration et al. 2018), Julia (Bezanson et al. 2017), numpy (Harris et al. 2020), scikit-image (Walt et al. 2014),

---

REFERENCES

Adams, W. S. 1915, Publications of the Astronomical Society of the Pacific, 27, 236, doi: 10.1086/122440

Astropy Collaboration, Price-Whelan, A. M., Sipőcz, B. M., et al. 2018, The Astronomical Journal, 156, 123, doi: 10.3847/1538-3881/aabc4f

Auwers, A. 1864, Monthly Notices of the Royal Astronomical Society, 25, 38. https://ui.adsabs.harvard.edu/abs/1864MNRAS..25...38A

Bessel, F. W. 1844, Monthly Notices of the Royal Astronomical Society, 6, 136, doi: 10.1093/mnras/6.11.136

Bezanson, J., Edelman, A., Karpinski, S., & Shah, V. B. 2017, SIAM Rev., 59, 65, doi: 10.1137/141000671

Blunt, S., Nielsen, E. L., De Rosa, R. J., et al. 2017, The Astronomical Journal, 153, 229, doi: 10.3847/1538-3881/aa6930

Bond, G. 1862, Astronomische Nachrichten, 57, 131. https://ui.adsabs.harvard.edu/abs/1862AN.....57..131B

Bond, H. E., Schaefer, G. H., Gilliland, R. L., et al. 2017, The Astrophysical Journal, 840, 70, doi: 10.3847/1538-4357/aa6af8

Bonnet-Bidaud, J.-M., & Pantin, E. 2008, A&A, 489, 651, doi: 10.1051/0004-6361:20078937

Bonsor, A., Farihi, J., Wyatt, M. C., & van Lieshout, R. 2017, Monthly Notices of the Royal Astronomical Society, 468, 154, doi: 10.1093/mnras/stx425

---

[1] https://github.com/mileslucas/sirius-b
[2] 10.5281/zenodo.5115225

Bottom, M., Ruane, G., & Mawet, D. 2017, Research Notes of the American Astronomical Society, 1, 30, doi: 10.3847/2515-5172/aa9d18

Burleigh, M. R., Clarke, F. J., & Hodgkin, S. T. 2002, Monthly Notices of the Royal Astronomical Society, 331, L41, doi: 10.1046/j.1365-8711.2002.05417.x

Collaboration, G., Prusti, T., de Bruijne, J. H. J., et al. 2016, Astronomy and Astrophysics, 595, A1, doi: 10.1051/0004-6361/201629272

Collaboration, G., Brown, A. G. A., Vallenari, A., et al. 2021, Astronomy and Astrophysics, 649, A1, doi: 10.1051/0004-6361/202039657

Cummings, J. D., Kalirai, J. S., Tremblay, P. E., & Ramirez-Ruiz, E. 2016, The Astrophysical Journal, 818, 84, doi: 10.3847/0004-637X/818/1/84

Cummings, J. D., Kalirai, J. S., Tremblay, P. E., Ramirez-Ruiz, E., & Choi, J. 2018, The Astrophysical Journal, 866, 21, doi: 10.3847/1538-4357/aadfd6

Fortney, J. J., Baraffe, I., & Militzer, B. 2010, Giant Planet Interior Structure and Thermal Evolution. https://ui.adsabs.harvard.edu/abs/2010exop.book..397F

Gatewood, G. D., & Gatewood, C. V. 1978, The Astrophysical Journal, 225, 191, doi: 10.1086/156480

Guizar-Sicairos, M., Thurman, S. T., & Fienup, J. R. 2008, Opt. Lett., OL, 33, 156, doi: 10.1364/OL.33.000156

Harris, C. R., Millman, K. J., van der Walt, S. J., et al. 2020, Nature, 585, 357, doi: 10.1038/s41586-020-2649-2

Hogan, E., Burleigh, M. R., & Clarke, F. J. 2009, Monthly Notices of the Royal Astronomical Society, 396, 2074, doi: 10.1111/j.1365-2966.2009.14565.x

Holman, M. J., & Wiegert, P. A. 1999, The Astronomical Journal, 117, 621, doi: 10.1086/300695

Huby, E., Bottom, M., Femenia, B., et al. 2017, Astronomy and Astrophysics, 600, A46, doi: 10.1051/0004-6361/201630232

Jeans, J. H. 1924, Monthly Notices of the Royal Astronomical Society, 85, 2, doi: 10.1093/mnras/85.1.2

Koester, D., Provencal, J., & Shipman, H. L. 1997, Astronomy and Astrophysics, v.320, p.L57-L59, 320, L57. https://ui.adsabs.harvard.edu/abs/1997A%26A...320L. .57K/abstract

Kuchner, M. J., & Brown, M. E. 2000, Publications of the Astronomical Society of the Pacific, 112, 827, doi: 10.1086/316581

Lucas, M., & Bottom, M. 2020, Journal of Open Source Software, 5, 2843, doi: 10.21105/joss.02843

Luhman, K. L., Burgasser, A. J., & Bochanski, J. J. 2011, The Astrophysical Journal, 730, L9, doi: 10.1088/2041-8205/730/1/L9

Marois, C., Lafrenière, D., Doyon, R., Macintosh, B., & Nadeau, D. 2006, The Astrophysical Journal, 641, 556, doi: 10.1086/500401

Mawet, D., Milli, J., Wahhaj, Z., et al. 2014, ApJ, 792, 97, doi: 10.1088/0004-637X/792/2/97

Nordhaus, J., & Spiegel, D. S. 2013, Monthly Notices of the Royal Astronomical Society, 432, 500, doi: 10.1093/mnras/stt569

Pairet, B. 2020, PhD thesis, UCL - Université Catholique de Louvain. https://dial.uclouvain.be/pr/boreal/object/boreal:240621

Pairet, B., Cantalloube, F., Gomez Gonzalez, C. A., Absil, O., & Jacques, L. 2019, Monthly Notices of the Royal Astronomical Society, 487, 2262, doi: 10.1093/mnras/stz1350

Pairet, B., Cantalloube, F., & Jacques, L. 2020, arXiv:2008.05170 [astro-ph]. http://arxiv.org/abs/2008.05170

Pathak, P., de la Roche, D. J. M. P. d., Kasper, M., et al. 2021, arXiv:2104.13032 [astro-ph]. http://arxiv.org/abs/2104.13032

Perets, H. B. 2010, arXiv e-prints, arXiv:1001.0581. https://ui.adsabs.harvard.edu/abs/2010arXiv1001.0581P

Probst, R. G. 1983, The Astrophysical Journal Supplement Series, 53, 335, doi: 10.1086/190893

Ren, B., Pueyo, L., Zhu, G. B., Debes, J., & Duchêne, G. 2018, The Astrophysical Journal, 852, 104, doi: 10.3847/1538-4357/aaa1f2

Schroeder, D. J., Golimowski, D. A., Brukardt, R. A., et al. 2000, The Astronomical Journal, 119, 906, doi: 10.1086/301227

Serabyn, E., Huby, E., Matthews, K., et al. 2017, The Astronomical Journal, 153, 43, doi: 10.3847/1538-3881/153/1/43

Skemer, A. J., & Close, L. M. 2011, The Astrophysical Journal, 730, 53, doi: 10.1088/0004-637X/730/1/53

Soummer, R., Pueyo, L., & Larkin, J. 2012, The Astrophysical Journal Letters, 755, L28, doi: 10.1088/2041-8205/755/2/L28

Telesco, C. M., Joy, M., & Sisk, C. 1990, The Astrophysical Journal, 358, L17, doi: 10.1086/185769

Thalmann, C., Usuda, T., Kenworthy, M., et al. 2011, The Astrophysical Journal, 732, L34, doi: 10.1088/2041-8205/732/2/L34

Traub, W. A., & Oppenheimer, B. R. 2010, Exoplanets, 111. http://adsabs.harvard.edu/abs/2010exop.book..111T

van den Bos, W. H. 1960, Journal des Observateurs, 43, 145. https://ui.adsabs.harvard.edu/abs/1960JO.....43..145V

576 van Dokkum, P. G. 2001, Publications of the Astronomical
577   Society of the Pacific, 113, 1420, doi: 10.1086/323894

578 Vanderburg, A., Rappaport, S. A., Xu, S., et al. 2020,
579   Nature, 585, 363, doi: 10.1038/s41586-020-2713-y

580 Veras, D. 2016, Royal Society Open Science, 3, 150571,
581   doi: 10.1098/rsos.150571

582 Vigan, A., Gry, C., Salter, G., et al. 2015, Monthly Notices
583   of the Royal Astronomical Society, 454, 129,
584   doi: 10.1093/mnras/stv1928

585 Walt, S. v. d., Schönberger, J. L., Nunez-Iglesias, J., et al.
586   2014, PeerJ, 2, e453, doi: 10.7717/peerj.453

587 Wizinowich, P. L., Acton, D. S., Lai, O., et al. 2000, 4007,
588   2, doi: 10.1117/12.390368

589 Xu, S., Ertel, S., Wahhaj, Z., et al. 2015, Astronomy
590   & Astrophysics, Volume 579, id.L8,
591   <NUMPAGES>5</NUMPAGES> pp., 579, L8,
592   doi: 10.1051/0004-6361/201526179

593 Yelda, S., Lu, J. R., Ghez, A. M., et al. 2010, The
594   Astrophysical Journal, Volume 725, Issue 1, pp. 331-352
595   (2010)., 725, 331, doi: 10.1088/0004-637X/725/1/331

596 Zuckerman, B., Melis, C., Klein, B., Koester, D., & Jura,
597   M. 2010, The Astrophysical Journal, 722, 725,
598   doi: 10.1088/0004-637X/722/1/725

APPENDIX

A. ADI PROCESSING RESULTS

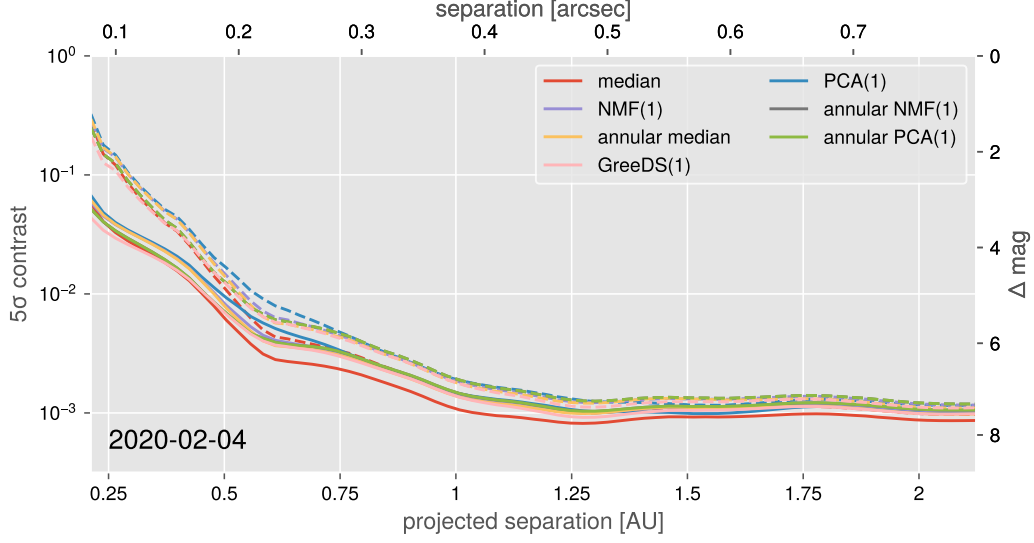**Figure 8.** 5σ contrast curves from every ADI algorithm for the first epoch. Both the Gaussian (solid lines) and Student-t corrected (dashed lines) contrast curves are shown.
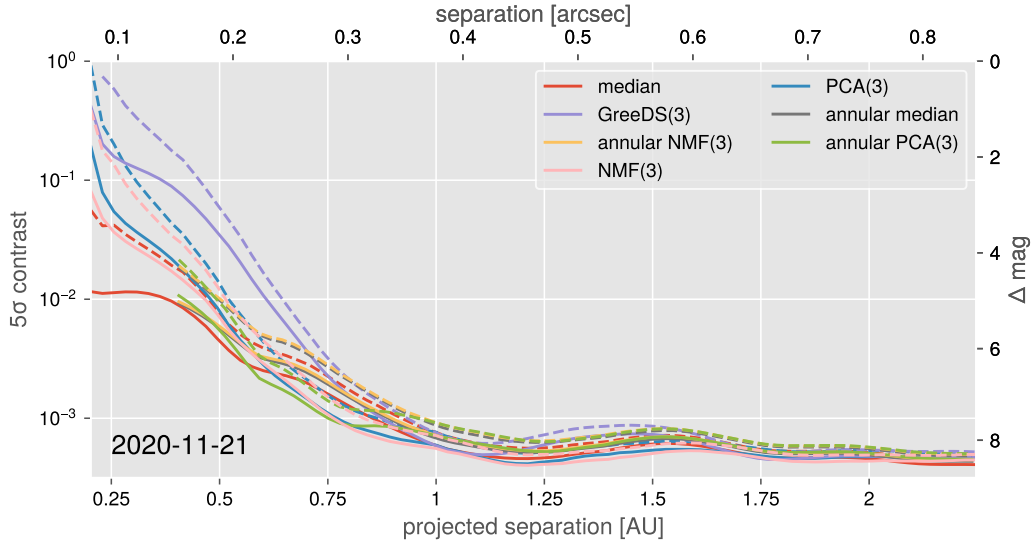

Figure 9. 5σ contrast curves from every ADI algorithm for the second epoch. Both the Gaussian (solid lines) and Student-t corrected (dashed lines) contrast curves are shown.

Fig. Set 10. **ADI processing results**

Fig. Set 11. **PCA, NMF, and GreeDS mosaics**

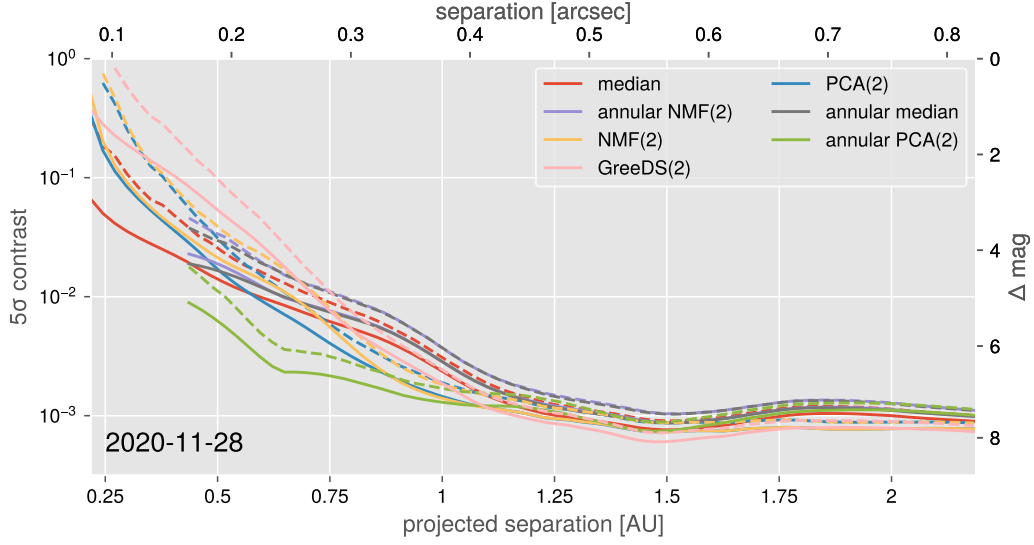**Fig. Set 12.** **PCA, NMF, and GreeDS results**

Figure 10. 5σ contrast curves from every ADI algorithm for the third epoch. Both the Gaussian (solid lines) and Student-t corrected (dashed lines) contrast curves are shown.
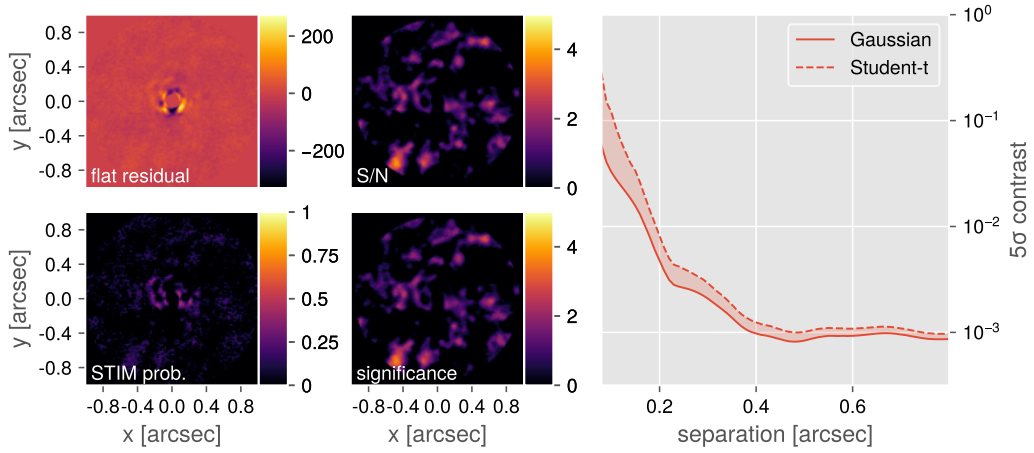

Figure 10. Post-processing results from the second epoch using full-frame median subtraction. The top-left frame is the collapsed residual frame, the top-right is the Gaussian S/N map, the bottom-left is the STIM probability map, and the bottom-right is the Student-t corrected significance map. In each frame the inner FWHM is masked out. The right figure show the Gaussian (solid line) and Student-t corrected (dashed curve) 5σ contrast curve. Outputs for other epochs and other algorithms (21 figures) are in the online figure set and the GitHub repository.
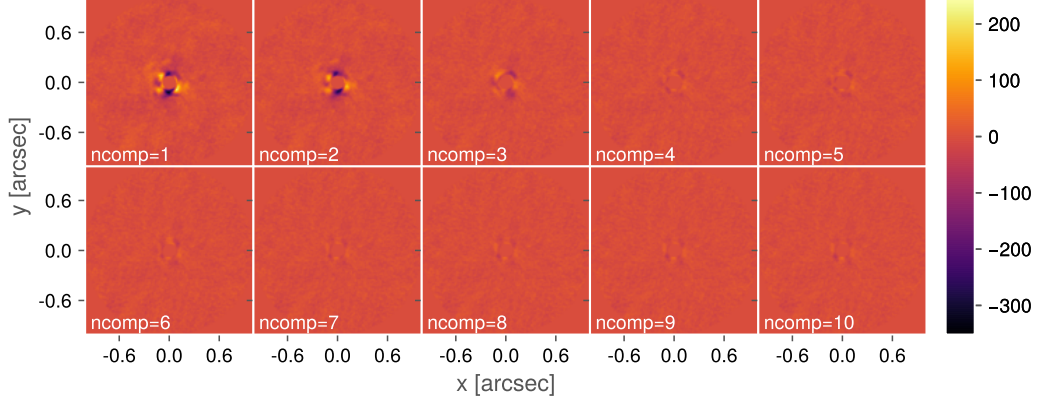
Figure 11. Collapsed residual frames from the first epoch using PCA reduction with 1-10 components. The figures share a common scale and the inner FWHM is masked out for all the frames. Outputs for the other epochs and for the NMF and GreeDS algorithms (9 figures) are in the online figure set and the GitHub repository
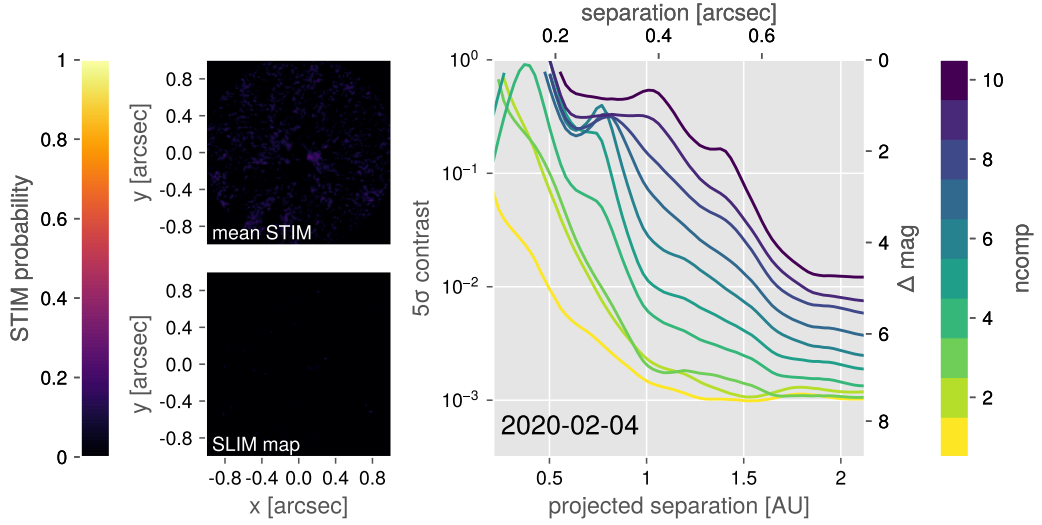

Figure 12. 5σ Gaussian contrast curves for the first epoch using PCA reduction with 1-10 components. The left two figures are the average STIM probability map, and the SLIM detection map. For both of these maps, a typical cutoff value is 0.5. Outputs for the other epochs and for the NMF and GreeDS algorithms (9 figures) are in the online figure set and the GitHub repository.

B. PROVISIONAL ORBIT FITTING

We found multiple interesting blobs in the reduced data that were not statistically significant. Nonetheless, we tried
fitting Keplerian orbits using OFTI to determine the feasibility of the blobs being real companions. We began by
estimating the astrometry of the blobs by eye in reduced data (table 3, fig. 14). We tried simulating 10^4 orbits via
rejection sampling with OFTI but no generated orbit was able to constrain all three points. Overall we determine
these blobs are not real companions and are most likely systematic noise in the stellar PSF.

Table 3. Provisional astrometry for a blob of interest from each epoch. The separation and offset are in relation to Sirius B. The uncertainties are derived from the FWHM of the PSF from each epoch.

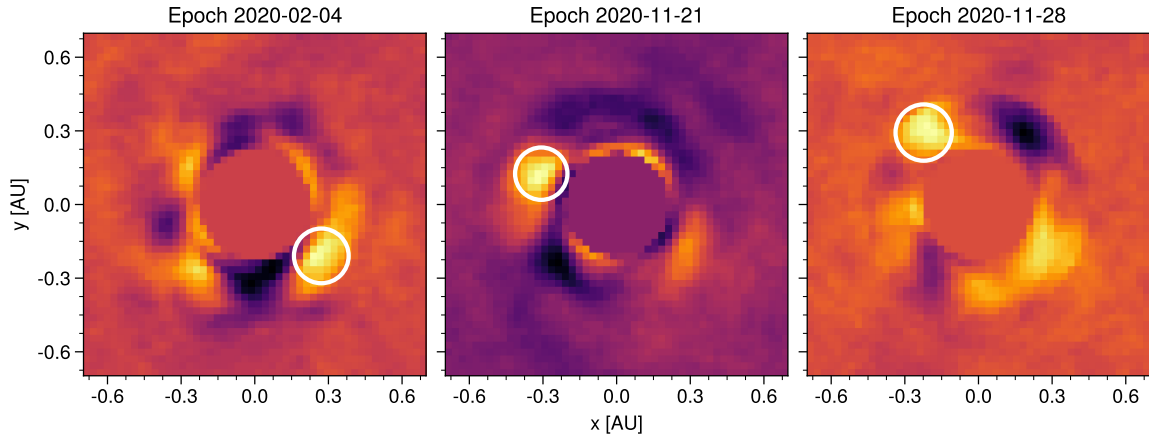| Date observed	offset (mas)	PA (°)
2020-02-04	123 ± 40	-128 ± 20
2020-11-21	119 ± 38	68 ± 18
2020-11-28	132 ± 41	37 ± 21

Figure 14. Provisional astrometry (white circles) displayed on collapsed and derotated residuals from each epoch. Each frame was cropped to the inner $\sim$0.7 AU (0.25″) and the inner FWHM has been masked out. The width of the circles represents the uncertainty.